

Numerical Study of Unsteady Distortion in an S-duct Intake Subjected to Blast Shock Waves

Longlong Shi[1,2], Yi Fan[1, 2] & Baigang Mi[1,2,*]

[1]School of Aeronautics, Northwestern Polytechnical University, Xi'an 710072, China
[2]National Key Laboratory of Aircraft Configuration Design, Xi'an, 710072, China
*Corresponding author. E-mail address: mibaigang@nwpu.edu.cn

Abstract

The S-duct intake has increasingly become a signature design feature of next-generation stealth fighter. As high-value military targets, these aircraft primarily face threats from air-to-air and surface-to-air missiles in combat environments. Blast shock waves generated by missile warheads are ingested into the S-duct and undergo intense interactions with the boundary layer. This process frequently induces large-scale flow separation and severe unsteady distortion at the Aerodynamic Interface Plane (AIP), leading to the deterioration of intake performance and jeopardizing the safety of the propulsion system. Therefore, evaluating the distortion characteristics of S-duct intakes under shock wave loading is critical for enhancing aircraft survivability. This paper aims to investigate the evolution of dynamic distortion in an S-duct intake subjected to shock-wave loading. The Pressurized Bubble Method (PBM) is employed to simulate blast shock-wave loads at different scaled distances. A numerical model including the S-duct intake and the first-stage compressor blade geometry is established, and a blade-resolved Multiple Reference Frame (MRF) simulation is adopted to investigate the propagation and reflection of the shock wave after entering the S-duct intake, as well as the induced dynamic distortion. The results show that after entering the intake, the shock wave undergoes multiple reflections on the curved walls and forms an upstream-propagating reflected shock wave in the blade region. Meanwhile, the interaction between the shock wave, boundary layer, and separated flow leads to pronounced transient non-uniformity in the total pressure distribution at the AIP, causing a rapid increase in the dynamic distortion level and strong unsteady fluctuations. The results provide a reference for analyzing the dynamic distortion mechanism of S-duct intakes under shock-wave loading, anti-distortion intake design, and propulsion system safety assessment.

Keywords: Shock wave; S-duct intake; Unsteady distortion; Blade-resolved MRF simulation

1. Introduction

The S-duct intake has become a signature design feature of next-generation stealth fighters because it can effectively shield the engine face and reduce the radar cross section[1]. However, owing to its curved duct and large-curvature configuration, internal boundary-layer separation and large-scale secondary flows are readily induced, leading to significant total-pressure distortion at the Aerodynamic Interface Plane (AIP) and threatening the stability of the engine. In combat environments, stealth fighters, as high-value military targets, face severe threats from air-to-air and surface-to-air missiles[2]. Once a missile warhead detonates near the aircraft, the generated strong shock wave may be ingested into the S-duct intake and interact intensely with the boundary layer and separated flow inside the duct. This transient interaction can further induce thrust fluctuations, reduce surge margin, and even cause compressor instability[3-5]. Therefore, investigating the exit flow quality and dynamic distortion characteristics of S-duct intakes under shock-wave loading is a key prerequisite for improving aircraft survivability and assessing propulsion system safety.

Extensive studies have been conducted on the evolution characteristics and damage effects of blast shock waves. In early blast engineering, free-field scaling laws and empirical overpressure correlations were commonly used as the primary tools for estimating the intensity of external shock

waves[6-8]. However, for blast problems involving complex confined spaces, empirical formulas are often unable to accurately describe highly nonlinear transient processes, such as shock-wave propagation, multiple reflections, and attenuation. With the rapid development of computational fluid dynamics (CFD), numerical simulation has become an important approach for investigating shock-wave dynamics in complex computational domains[9-12]. In CFD modeling of shock waves, conventional detonation-product modeling methods usually employ the JWL equation of state to describe the expansion process of detonation products, which can realistically simulate near-field detonation-product driving and shock-wave formation. However, this approach imposes high requirements on mesh resolution, time-step size, and computational resources[13]. In contrast, the Pressure Bubble Method (PBM)[14], as a simplified modeling approach that represents the energy released by an explosion as the release of internal energy from a high-pressure bubble, can efficiently and accurately simulate the shock-wave propagation profile and overpressure characteristics in the flow field while avoiding complex detonation-reaction calculations.

Although the interaction between shock waves and complex structures has attracted considerable attention in the aerospace field, existing studies on blast shock waves have mainly focused on the dynamic response and damage assessment of aircraft structures subjected to external shock loading[15-16]. In terms of internal aerodynamics, existing distortion studies have generally focused on the intrinsic distortion induced by the geometric curvature of the intake itself[17-18]. However, when an external transient shock wave enters a complex serpentine duct, the complicated reflection mechanism on the curved walls, its strong coupling with internal unsteady separated flow, and the resulting severe dynamic distortion evolution at the AIP have not yet been systematically revealed.

To address the above research gap, this study aims to investigate the evolution characteristics and physical mechanisms of dynamic distortion in an S-duct intake subjected to shock-wave loading. The Pressure Bubble Method (PBM) is employed to equivalently simulate blast shock-wave loads at different scaled distances, and a three-dimensional numerical model including the S-duct intake and the realistic geometry of the first-stage compressor blades is established. In the numerical simulation, the three-dimensional compressible Unsteady Reynolds-Averaged Navier–Stokes (URANS) equations are solved, and a blade-resolved Multiple Reference Frame (MRF)-based unsteady simulation method is adopted. This approach avoids the high computational cost associated with sliding-mesh simulations while effectively capturing the propagation and reflection of the shock wave in the curved duct, as well as its interaction with the first-stage blade region. By analyzing the transient non-uniformity of the flow field after shock-wave ingestion and the strong fluctuations of dynamic distortion at the AIP, this study reveals the influence of shock-wave intensity on the intake-exit flow quality. The results provide theoretical support for understanding the dynamic distortion mechanism of S-duct intakes under shock-wave loading and offer an important reference for anti-distortion intake design and propulsion system safety assessment.

2. Numerical Method and Case Validation

This section mainly presents the numerical methods adopted in this study and their validation procedures. First, the unsteady numerical simulation method for the S-duct intake is introduced, including the governing equations, turbulence model, and discretization schemes. Its reliability is then validated by comparing the numerical results of the M2129 intake case with experimental data. Second, the basic setup of the Pressurized Bubble Method (PBM) is described, and its applicability for simulating blast shock waves is verified by comparison with ideal detonation results.

2.1 Unsteady Numerical Simulation Method

The flow field was solved using the commercial CFD software STAR-CCM+[19]. The governing equations are the three-dimensional compressible URANS equations in a Cartesian coordinate system, and their integral conservation form[20] can be written as:

$$\frac{\partial}{\partial t}\iiint \boldsymbol{Q} dV + \iint \boldsymbol{f}\cdot\boldsymbol{n} dS = 0 \tag{1}$$

where V is the control volume, S is the surface area of the control volume, $\boldsymbol{Q}$ is the vector of conserved variables, $\boldsymbol{f}$ represents the net flux vector—including both inviscid and viscous fluxes

through surface S, and $\boldsymbol{n}$ denotes the unit outward normal vector to the surface.

An implicit unsteady scheme is used for time discretization, with a second-order temporal discretization for the unsteady terms. A second-order upwind scheme is adopted for spatial discretization. Considering the strong unsteady interactions among the shock wave, the boundary layer, separated flow, and blade passages inside the intake, the $k-\omega\ SST$ turbulence model[21] is employed. This model provides good near-wall accuracy while maintaining stability in the outer flow region, and is suitable for complex internal flows involving adverse pressure gradients, flow separation, and shock-wave/boundary-layer interactions.

To validate the reliability of the numerical simulation method described above, the M2129 S-duct intake designed by the AGARD group is adopted[22]. Wind-tunnel experiments for this intake were conducted with the support of NASA. As shown in Figure 1, the M2129 intake is shown in gray, while the far-field boundary is shown in black. The far-field region consists of a hemispherical domain, with a diameter 30 times that of the intake exit. The far-field boundary is defined as a freestream boundary condition, the intake wall is defined as a no-slip wall boundary condition, and the intake exit is defined as a pressure outlet boundary condition. The meshes on the far-field boundary, intake wall, and symmetry plane of the computational domain are shown in Figure 2.

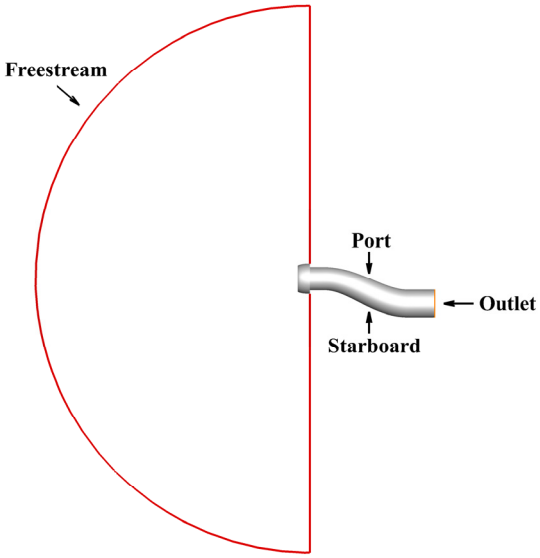


Figure 1 –Computational domain of M2129.

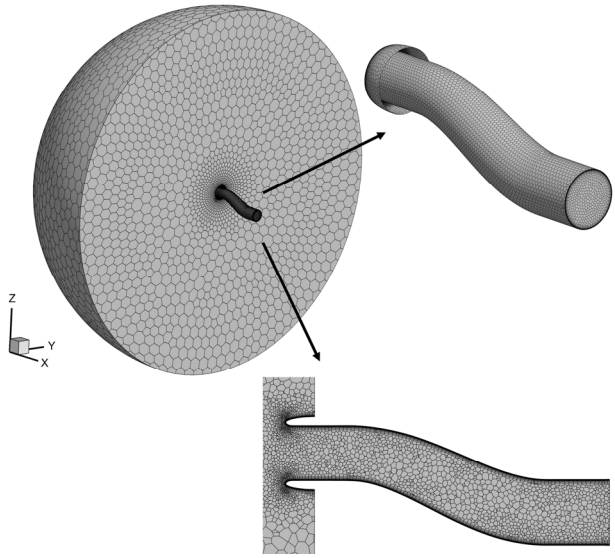
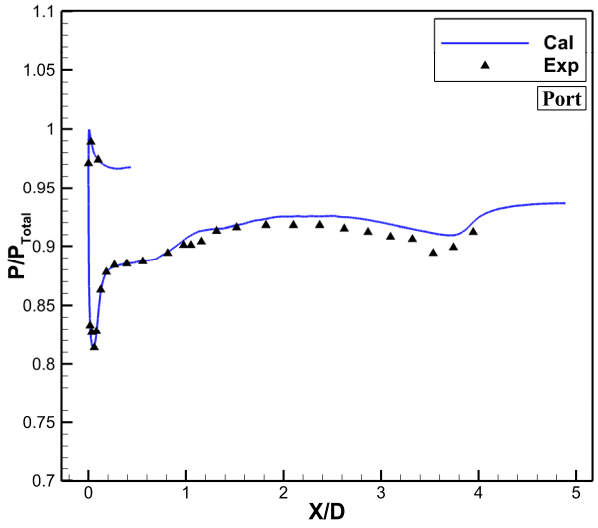
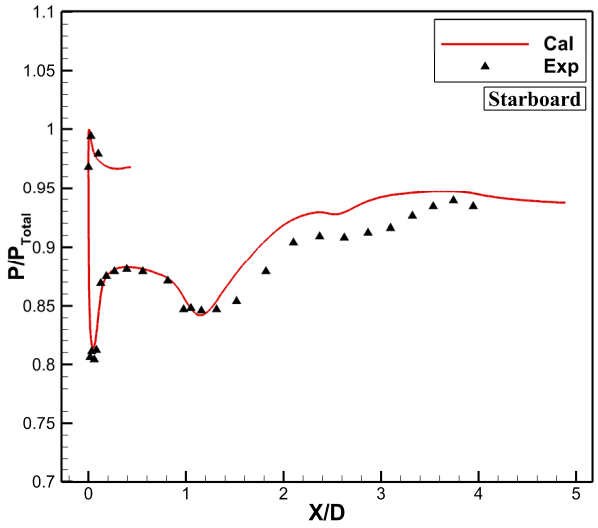


Figure 2 –Mesh of the computational domain.

The computational condition is set as follows: the freestream conditions of the domain were given as a 0.21 Mach number, total pressure $P_T = 101146Pa$, and total temperature $T_T = 292.78K$. A pressure $P = 95009.8Pa$ was applied to the outlet of the domain (AIP).



(a) Port



(b) Starboard

Figure 3 – Static pressure ratio along the port and starboard sides.

Figure 3 compares the calculated results (Cal) and wind-tunnel experimental data (Exp) of the static pressure ratio (P / P_{Total}) on the port and starboard sides of the M2129 intake. It can be seen that the calculated pressure distribution on the port side agrees well with the experimental data. For the starboard side, the calculated values are slightly higher than the experimental data, but the discrepancy remains small. Overall, the numerical results can reasonably predict the wall static pressure distribution of the M2129 intake, thereby validating the reliability of the numerical simulation method used in this study.

2.2 Pressurized Bubble Method

The Pressurized Bubble Method (PBM) is a simplified modeling approach in which the energy released by an explosion is equivalently represented by the release of internal energy from a high-pressure air bubble. It is suitable for free-field shock-wave propagation, far-field overpressure estimation, and blast load analysis. The PBM adopted in this study follows the constant-volume condition described by Blanc et al[23]. The high-pressure bubble is assumed to be a sphere with a radius of r_b, in which the air density and specific internal energy are ρ_b and e_b, respectively. The density and specific internal energy of the ambient air are ρ_0 and e_0, respectively. Therefore, the effective releasable energy E_b of the bubble can be expressed as:

$$E_b = \frac{4}{3}\pi r_b^3 \left(\rho_b e_b - \rho_0 e_0\right) \tag{2}$$

By equating the bubble energy to the TNT-equivalent energy, the energy-equivalence formula for the PBM can be obtained:

$$\frac{4}{3}\pi r_b^3 \frac{P_b - P_0}{\gamma - 1} = e_{TNT} m_{TNT} \tag{3}$$

The pressurized bubble resulting from an isochoric compression in which the specific energy is set to that of TNT:

$$e_b = e_{TNT} \tag{4}$$

$$\rho_b = \frac{P_b}{(\gamma - 1) e_b} \tag{5}$$

The computational domain for the PBM is divided into two regions: the air region and the pressure bubble, as shown in Figure 4. A high pressure and high temperature are imposed on the pressurized gas region until the density inside the bubble reaches the value given by Equation (5). The temperature inside the bubble is given by:

$$T_b = \frac{(\gamma - 1) e_b}{R} \tag{6}$$

To validate the reliability of the PBM, a free-air explosion of 1 kg TNT is selected. The overpressure variation at the scaled distance of Z=2 is monitored, and the overpressure predicted by the PBM is compared with that obtained from a conventional ideal TNT detonation simulation using the JWL equation of state. The scaled distance is defined as:

$$Z = \frac{R_m}{W^{1/3}} \tag{7}$$

where R_m is the distance between the monitoring point and the explosion center in meters, and W is the equivalent TNT charge mass in kilograms.

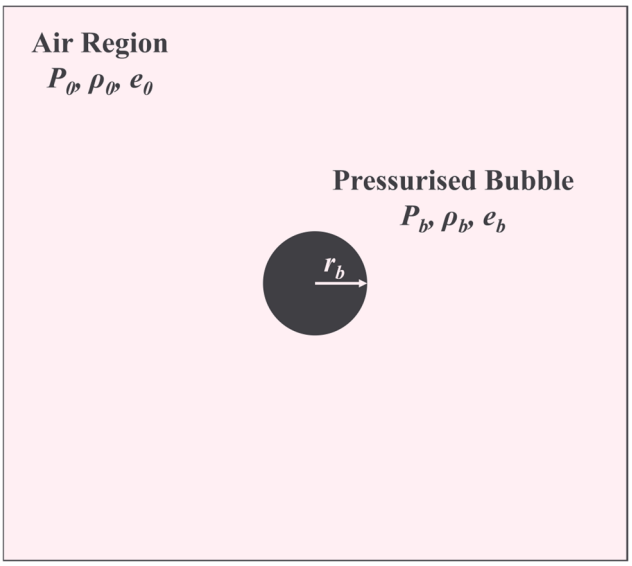


Figure 4 –Schematic diagram of the PBM.

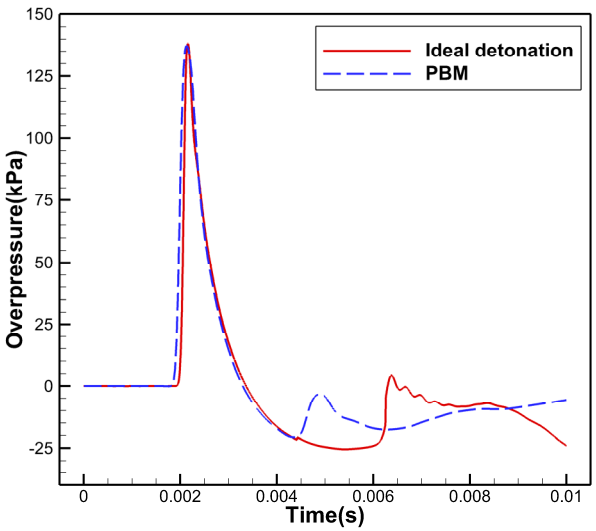


Figure 5 –Comparison of overpressure between ideal detonation and the PBM.

Figure 5 shows the comparison of the overpressure time histories obtained using the ideal detonation model and the PBM. It can be seen that the PBM can reasonably reproduce the overall characteristics of the shock-wave overpressure profile, and the peak overpressure agrees well with the ideal detonation result. Only a slight discrepancy is observed in the arrival time of the secondary shock wave. Therefore, the PBM is capable of effectively simulating the propagation process of blast shock waves.

3. Case Analysis of Dynamic Distortion in an S-Duct Intake Subjected to Shock Waves

3.1 Simulation Procedure

The schematic diagram and flowchart for simulating dynamic distortion in an S-duct intake under shock-wave loading are shown in Figures 6 and 7, respectively. First, the Pressurized Bubble Method (PBM) is used to equivalently simulate the blast shock-wave load. According to the prescribed TNT equivalent and scaled distance, the initial pressure P_b and initial temperature T_b of the pressurized bubble region are calculated and imposed in the computational domain as the initial condition for the blast shock wave. Through the rapid expansion of the high-pressure bubble, an outward-propagating shock wave is generated in the free field, thereby representing the shock-wave load produced by the explosion.

Second, a three-dimensional numerical model including the S-duct intake and the first-stage compressor blade region is established. For the first-stage compressor blade region, a blade-resolved Multiple Reference Frame (MRF) method[24] is employed to represent the rotational effect of the blades. In this method, the blade geometry is explicitly modeled, and the flow within the blade passages is solved in a rotating reference frame and coupled with the stationary S-duct intake region. This treatment accounts for the influence of blade rotation on the intake distortion response while avoiding the high computational cost of a sliding-mesh approach. Thus, the unsteady interaction between the shock wave entering the intake and the first-stage blade region can be simulated.

After the geometric model is established, the computational domain is meshed. Mesh refinement is applied to key regions, including the curved intake walls, boundary-layer development regions, the AIP section, and blade leading edges, to ensure the capability of capturing shock-wave propagation, wall reflection, flow separation, and the AIP distortion distribution. The boundary conditions are then specified, including the far-field freestream condition, no-slip wall condition for the intake walls, pressure outlet condition for compressor exit, and parameters of the MRF rotating region.

Finally, three-dimensional unsteady simulations are performed. After the shock wave generated by the PBM enters the S-duct intake, it propagates through the curved duct and interacts with the intake walls, boundary layer, separated flow, and first-stage blade region. The unsteady calculation provides the temporal evolution of the pressure, velocity, and density fields inside the intake under shock-wave loading, allowing the propagation, reflection, and attenuation characteristics of the shock wave within the intake to be analyzed. On this basis, the total pressure distribution and dynamic

distortion parameters at the AIP are extracted to further evaluate the influence of shock-wave loading on the exit flow quality and dynamic distortion characteristics of the S-duct intake.

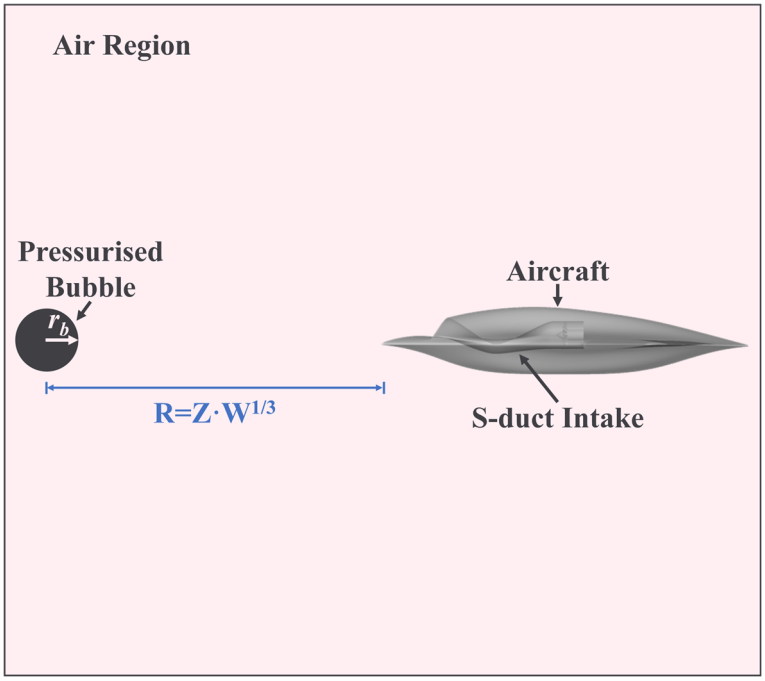


Figure 6 – Schematic diagram of the simulation.

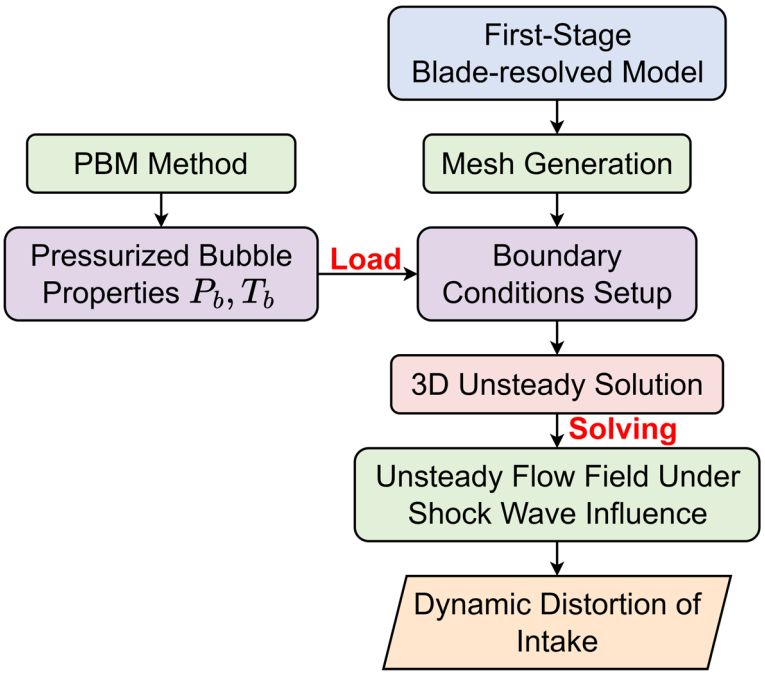


Figure 7 – Flowchart of the simulation.

3.2 Physical Model and Mesh Generation

The research object is a flying-wing aircraft with an S-duct intake. The model is symmetric about the center plane. Its planform geometry is shown in Figure 8, and the geometries of the S-duct intake and the first-stage compressor blades are shown in Figure 9. And the diameter of the intake exit is 0.9 m.

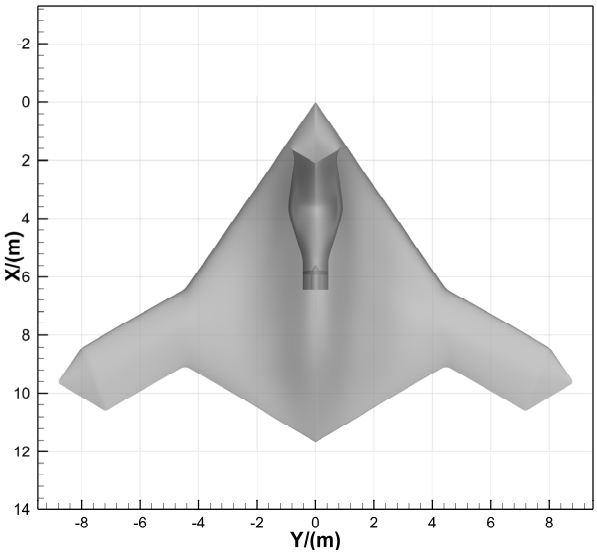


Figure 8 –Schematic diagram of the PBM.

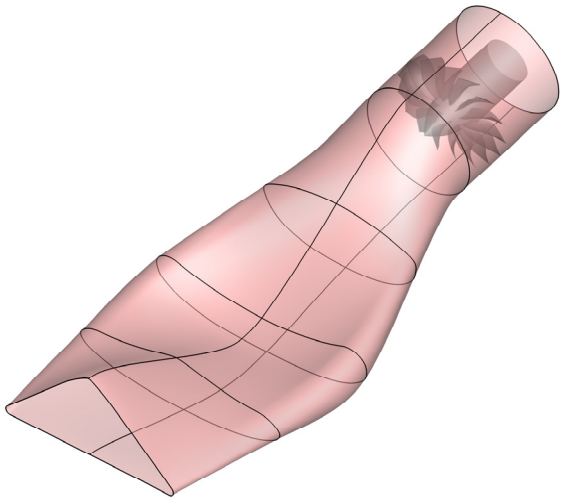


Figure 9 –Schematic diagram of the PBM.

A polyhedral unstructured mesh is adopted for the computational domain. To improve the resolution of key flow structures, local mesh refinement is applied to the intake walls, the AIP section, and the first-stage compressor blade region. In addition, 25 prism layers are generated near the walls, and the height of the first near-wall cell satisfies $Y^+ \leq 1$. The total number of cells in the computational domain is approximately 15 million. The meshes on the aircraft surface, intake walls, and first-stage compressor blade region are shown in Figure 10.

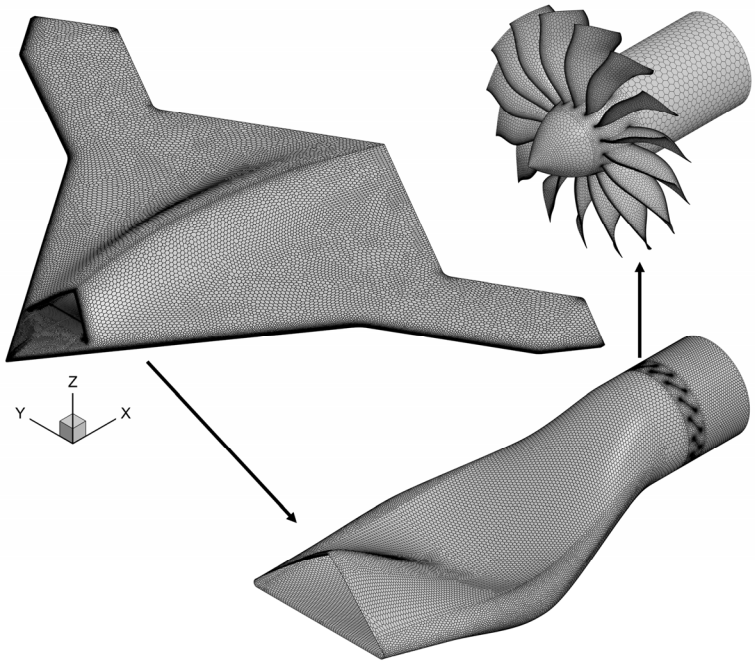


Figure 10 – Flowchart of the simulation.

In the simulation, the freestream is set to $Ma = 0.6$, $P_0 = 26500Pa$, $T_0 = 223.25K$. And the rotational speed of the first-stage compressor blades is $6500\ rpm$. The TNT equivalent of the explosive is 10 kg, and the initial air pressure inside the pressurized bubble is set to $10^7\ Pa$. According to Equation (3), the radius of the pressurized bubble is calculated to be $0.766\ m$, and according to Equation (6), the initial temperature of the pressurized bubble is calculated to be $6550\ \mathrm{K}$. Numerical simulations of dynamic distortion in the S-duct intake under shock-wave loading are then conducted for two scaled-distance cases, Z=2 and Z=5.

In this study, the circumferential steady total-pressure distortion index DC_θ is adopted as the evaluation parameter for intake-exit distortion. This index can effectively reflect both the circumferential extent and the intensity of distortion at the intake exit. In addition, the mean dynamic pressure of the flow field is introduced to account for the influence of velocity distribution on the

distortion evaluation. A smaller value of this index indicates a more uniform circumferential distribution of total pressure at the intake exit and a lower level of outlet flow distortion. The index is defined as follows:

$$DC_\theta = \frac{p_{t,av} - p_{t,\theta}}{q_{av}}, q_{av} = \rho V^2/2 \tag{8}$$

where $p_{t,\theta}$ is the minimum circumferentially averaged total pressure in the θ-degree sector at the intake exit, and q_{av} is the average dynamic pressure at the intake-exit plane.

3.3 Scaled Distance Z=2

To analyze the influence of strong shock waves at a smaller scaled distance on the dynamic distortion characteristics of the S-duct intake, the case with a scaled distance of Z=2 is selected in this section. The propagation and reflection of the shock wave after entering the intake, as well as the distortion evolution at the AIP, are investigated. The simulation time step is set to $2.5\times10^{-5}s$, and the simulation stop time is $0.05s$.

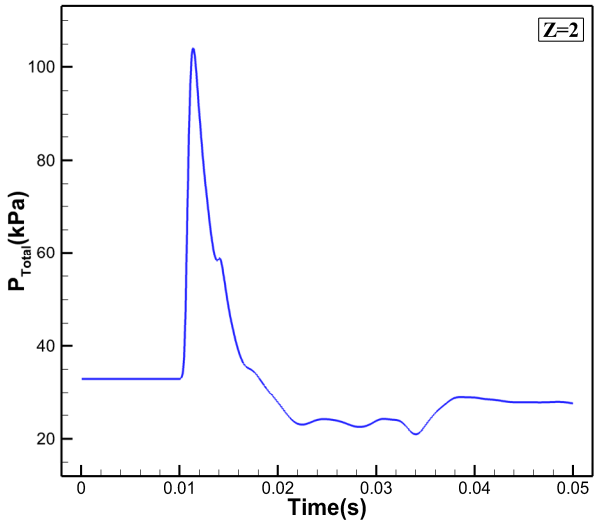


Figure 11 –Average total pressure at the AIP.

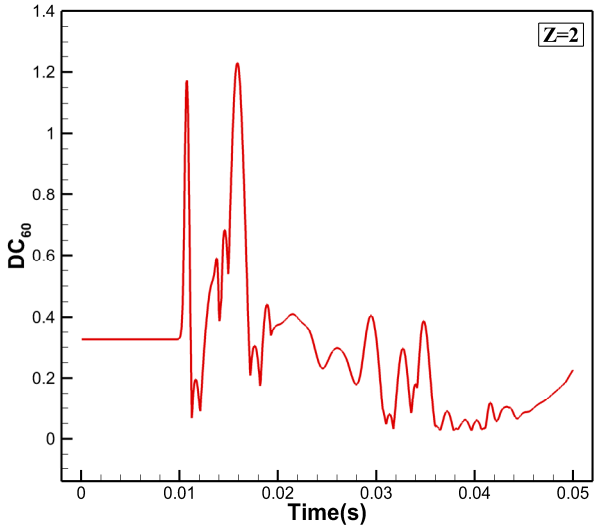
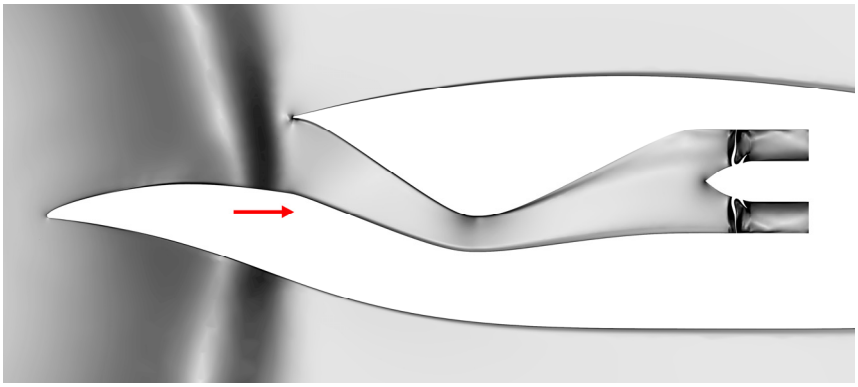
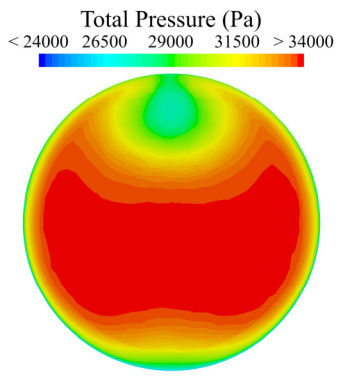


Figure 12 –DC_{60} at the AIP.

Figures 11 and 12 show the time histories of the average total pressure and DC_{60} at the AIP for the scaled-distance case of Z=2, respectively. It can be seen that before the shock wave reaches the intake, the average total pressure at the AIP remains nearly stable, and DC_{60} is maintained at a relatively low level, indicating that the intake-exit flow field is in a relatively stable state. When the shock wave reaches the AIP at approximately t=0.01s, the average total pressure at the AIP increases rapidly and reaches a peak within a short time, indicating that the shock wave induces a significant transient compression effect after entering the intake. Subsequently, the average total pressure decreases rapidly and exhibits fluctuations of a certain amplitude, suggesting that the propagation and reflection of the shock wave inside the intake, together with its interaction with the blade region, result in pronounced unsteady variations in the exit pressure field. Corresponding to the variation in the average total pressure, DC_{60} increases rapidly after the arrival of the shock wave and reaches a second peak at t=0.01075s, indicating that strong circumferential non-uniformity of the total pressure distribution is generated at the AIP under shock-wave loading. As the shock wave continues to propagate and gradually attenuates, DC_{60} shows an overall decreasing trend, but obvious oscillations still exist. This indicates that the dynamic distortion at the intake exit does not recover immediately, but continues to evolve under the combined effects of shock-wave reflection, separated-flow development, and disturbances from the blade region.

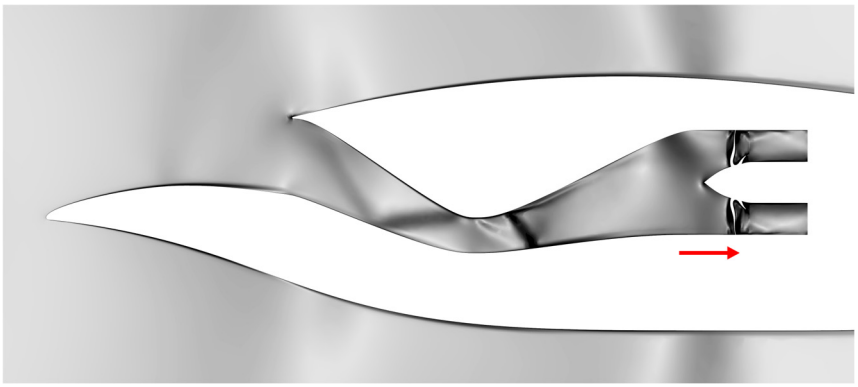


(a) Numerical Schlieren image on the symmetry plane

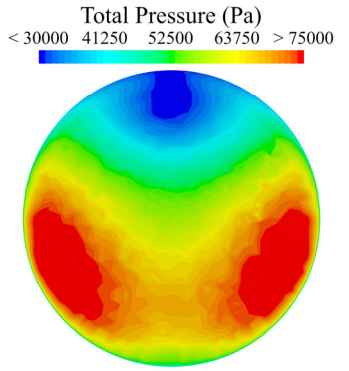


(b) P_{Total} distribution at AIP

Figure 13 – Time=0.005s.

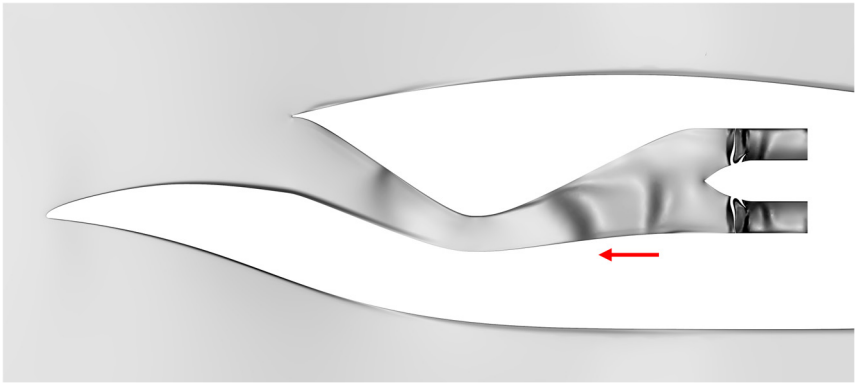


(a) Numerical Schlieren image on the symmetry plane

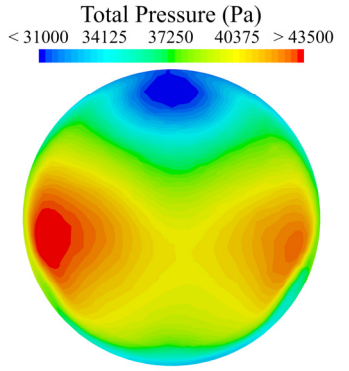


(b) P_{Total} distribution at AIP

Figure 14 – Time=0.01075s.

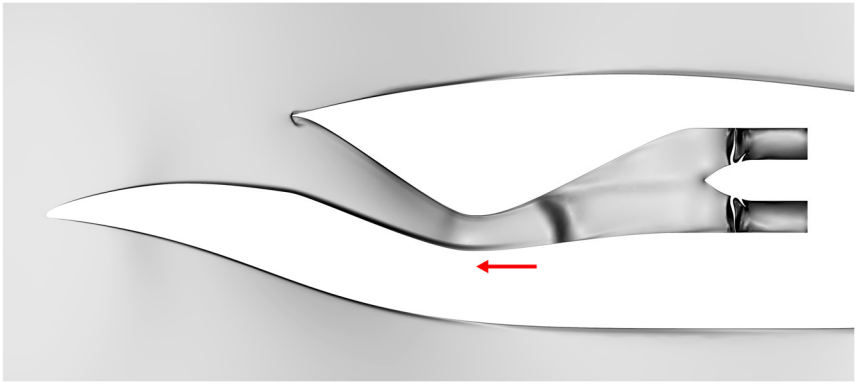


(a) Numerical Schlieren image on the symmetry plane

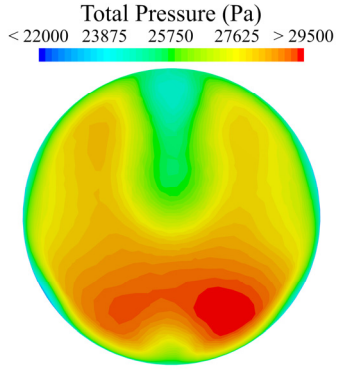


(b) P_{Total} distribution at AIP

Figure 15 – Time=0.0159s.

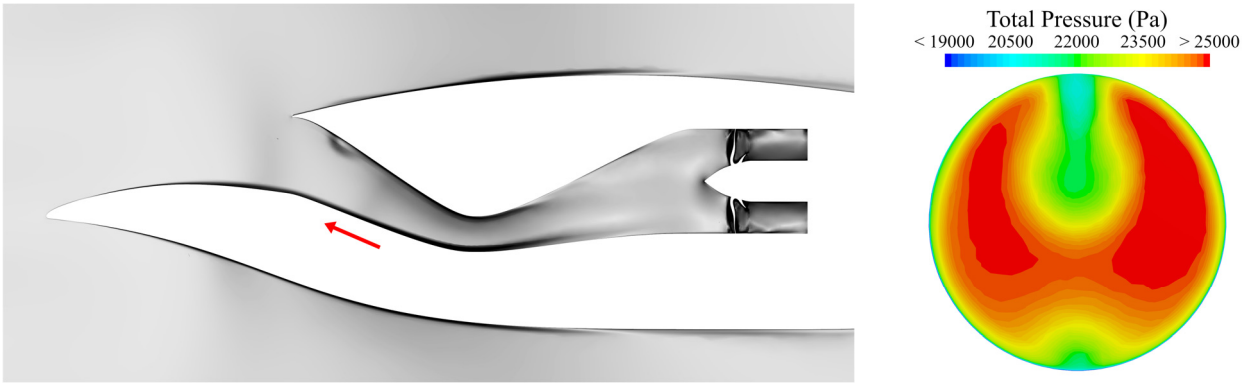


(a) Numerical Schlieren image on the symmetry plane



(b) P_{Total} distribution at AIP

Figure 16 – Time=0.02s.



(a) Numerical Schlieren image on the symmetry plane (b) P_{Total} distribution at AIP

Figure 17 – Time=0.025s.

Figures 13–17 further present the numerical Schlieren images[25] on the symmetry plane and the total pressure distributions at the AIP at different time instants, which are used to analyze the propagation process of the shock wave in the S-duct intake and the resulting dynamic distortion characteristics. At t=0.005s, the shock wave has not yet entered the intake and propagates toward the intake entrance along the direction indicated by the arrow. At this moment, the total pressure distribution at the AIP remains relatively stable, mainly showing the total pressure non-uniformity caused by the curved flow path and boundary-layer development in the S-duct intake itself, and the dynamic distortion level is relatively low.

At t=0.01075s, the incident shock wave enters the intake and propagates downstream through the curved duct, reaching the fan region. Owing to the large curvature of the S-duct intake, the shock wave interacts with the intake walls and boundary layer during its propagation, resulting in the formation of multiple shock structures. At this time, the total pressure distribution at the AIP changes significantly. A distinct low-total-pressure region appears in the upper part of the section, while relatively high total pressure is observed on both sides, indicating that the shock wave significantly enhances the circumferential total-pressure distortion at the intake exit. This moment corresponds to the rapid increase in the average total pressure and the sharp rise in DC_{60} in Figures 11-12.

At t=0.0159s, the shock wave interacts with the first-stage compressor blade region, producing complex reflections. Part of the reflected shock wave starts to propagate upstream, as indicated by the arrow in the figure. The total pressure distribution at the AIP still exhibits strong non-uniformity, and the high- and low-total-pressure regions show a clearly asymmetric distribution. This is mainly attributed to the non-uniform circumferential disturbances induced by the blade rotational effect. This phenomenon indicates that the reflection effect of the blade region maintains the dynamic distortion at a relatively high level. This moment corresponds to the second peak of DC_{60} in Figure 12.

After t=0.02s, the reflected shock wave continues to propagate upstream. Under the influence of the curved walls and separated flow, the reflected shock structure is deformed and attenuated within the duct. The corresponding total pressure distributions at the AIP show that, as the reflected shock wave gradually moves away from the blade region, the exit total pressure distribution recovers to some extent compared with the strong shock-wave interaction stage. However, obvious high- and low-total-pressure non-uniformity still exists within the section, and the distortion pattern continues to vary with time.

Overall, under the Z=2 condition, the shock wave is relatively strong. After entering the S-duct intake, it not only causes severe transient variations in the average total pressure at the AIP, but also leads to a rapid increase and sustained oscillation of the AIP dynamic distortion level through wall reflection, blade-region reflection, and interaction with the separated flow. As a result, the flow quality at the intake exit is significantly deteriorated.

3.4 Scaled Distance Z=5

To analyze the influence of strong shock waves at a moderate scaled distance on the dynamic distortion characteristics of the S-duct intake, the case with a scaled distance of Z=5 is selected in this section. The propagation and reflection of the shock wave after entering the intake, as well as

the distortion evolution at the AIP, are investigated. The simulation time step is set to $2.5\times10^{-5}s$, and the simulation stop time is $0.05s$.

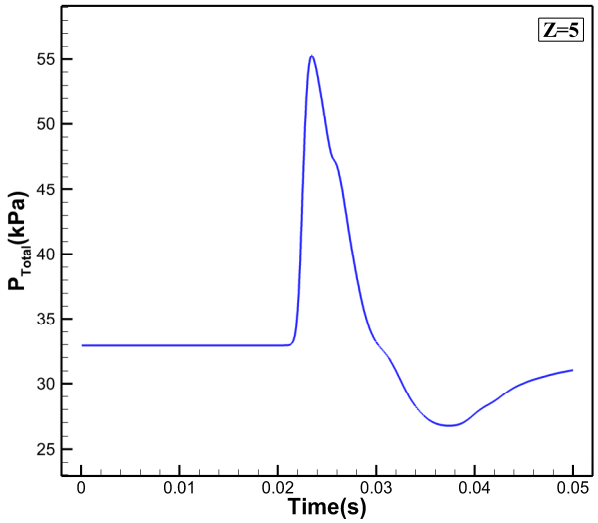


Figure 18 –Average total pressure at the AIP.

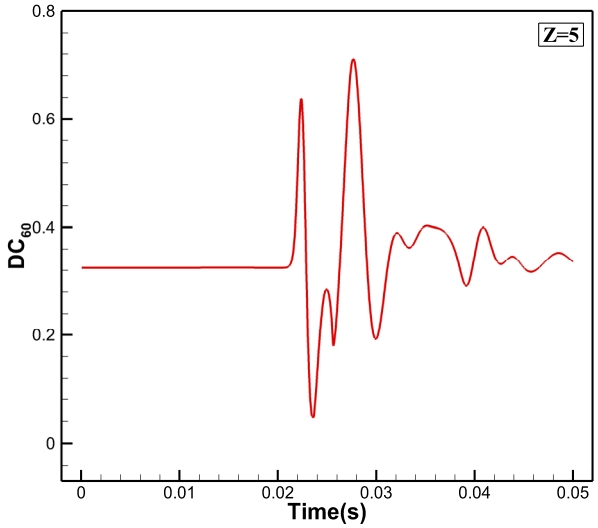
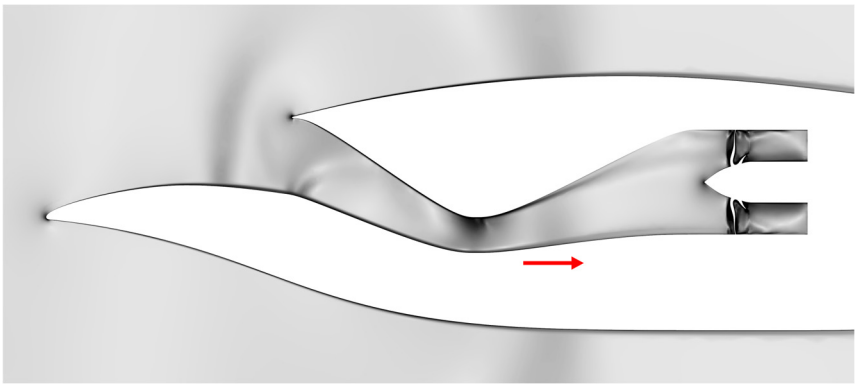
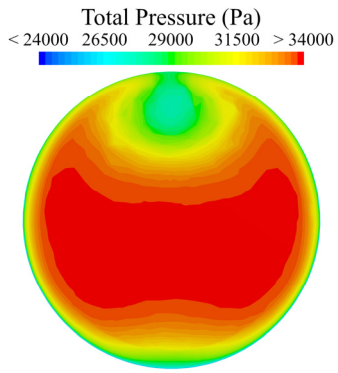


Figure 19 –DC_{60} at the AIP.

Figures 18-19 show the time histories of the average total pressure and DC_{60} at the AIP for the scaled-distance case of Z=5, respectively. It can be seen that before the shock wave reaches the intake, the average total pressure at the AIP remains nearly stable, and DC_{60} is maintained at a relatively low level, indicating that the intake-exit flow field is in a relatively stable state. When the shock wave reaches the vicinity of the AIP at approximately t=0.0224s, the average total pressure at the AIP increases rapidly and reaches a peak within a short time, indicating that the shock wave induces a noticeable transient compression effect after entering the intake. Subsequently, the average total pressure gradually decreases and exhibits certain fluctuations, suggesting that the propagation and reflection of the shock wave inside the intake, together with its interaction with the blade region, result in unsteady variations in the exit pressure field. Corresponding to the variation in the average total pressure, DC_{60} fluctuates rapidly after the shock-wave impact and reaches peaks at t=0.0224s and t=0.0277s, indicating that pronounced circumferential non-uniformity of the total pressure distribution is generated at the AIP. Compared with the Z=2 case, both the peak average total pressure and the peak DC_{60} at the AIP are significantly lower in the Z=5 case, indicating that the shock-wave intensity decreases with increasing scaled distance, and its influence on the dynamic distortion at the intake exit is relatively reduced.

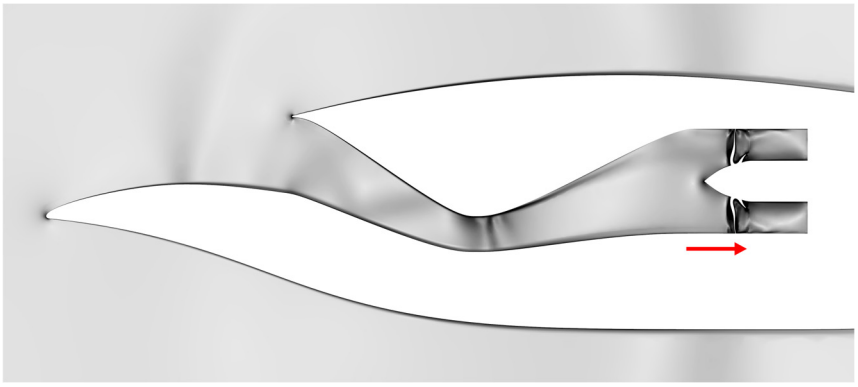


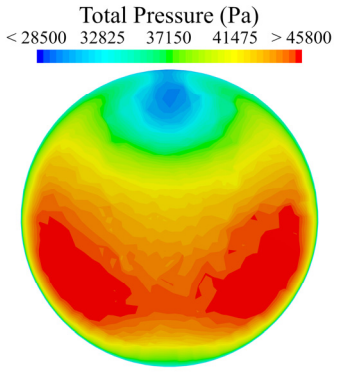
(a) Numerical Schlieren image on the symmetry plane



(b) P_{Total} distribution at AIP

Figure 20 – Time=0.02s.

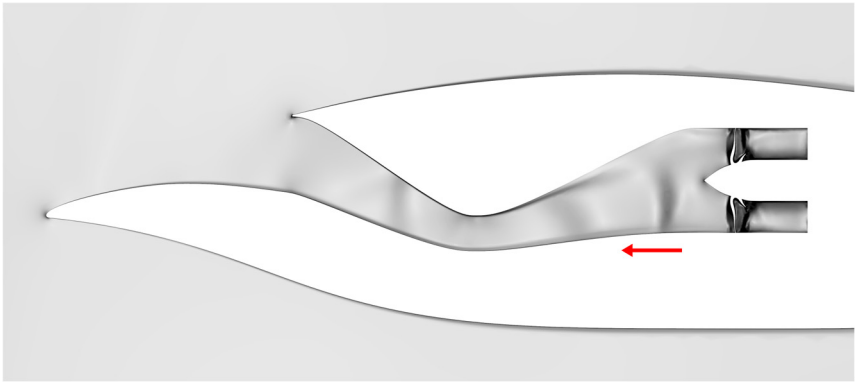


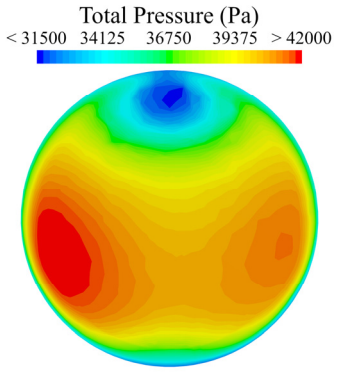


(a) Numerical Schlieren image on the symmetry plane

(b) P_{Total} distribution at AIP

Figure 21 – Time=0.0224s.

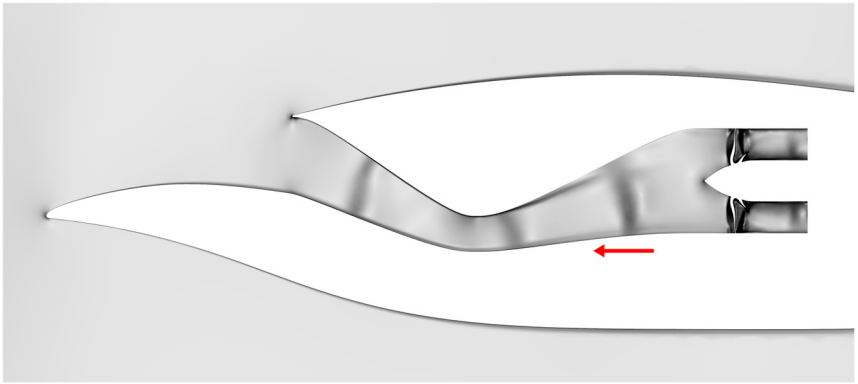


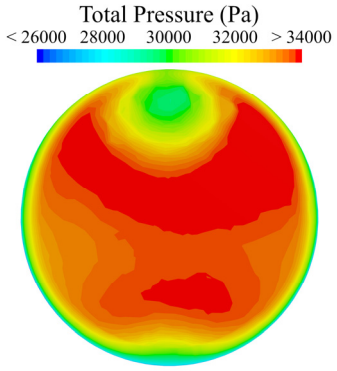


(a) Numerical Schlieren image on the symmetry plane

(b) P_{Total} distribution at AIP

Figure 22 – Time=0.0277s.

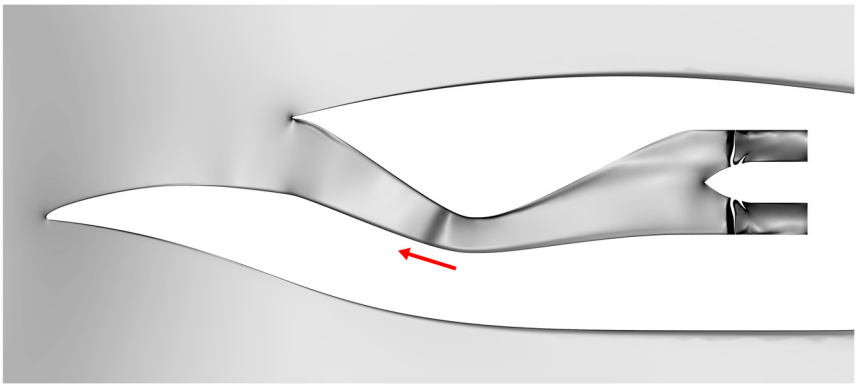


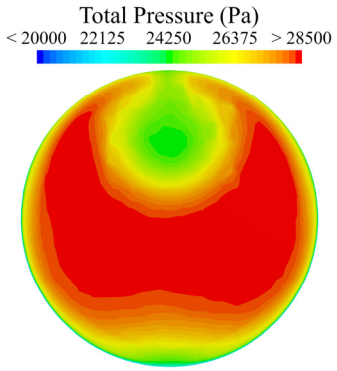


(a) Numerical Schlieren image on the symmetry plane

(b) P_{Total} distribution at AIP

Figure 23 – Time=0.03s.





(a) Numerical Schlieren image on the symmetry plane

(b) P_{Total} distribution at AIP

Figure 24 – Time=0.04s.

Figures 20–24 further present the numerical Schlieren images on the symmetry plane and the total pressure distributions at the AIP at different time instants, which are used to analyze the propagation and reflection processes of the shock wave in the S-duct intake under the Z=5 condition. At t=0.02s, the shock wave has entered the S-duct intake but has not yet reached the AIP, and the dynamic distortion has not been significantly enhanced.

At t=0.0224s, the shock wave approaches the blade region. During its propagation, the shock wave interacts with the curved walls and boundary layer, enhancing the flow disturbance inside the intake. At this time, the total pressure distribution at the AIP begins to change noticeably. A low-total-pressure region appears in the upper part of the section, while relatively high total pressure is observed on both sides, indicating that the shock-wave effect begins to intensify the circumferential total-pressure distortion at the intake exit. This stage corresponds to the rapid increase in the average total pressure at the AIP in Fig. 18 and the first peak of DC_{60} in Fig. 19.

At t=0.0277s, the shock wave interacts with the first-stage compressor blade region and produces reflections. Part of the reflected shock wave starts to propagate upstream, as indicated by the arrow in the figure. At this moment, the total pressure distribution at the AIP exhibits obvious non-uniformity. This time instant corresponds to the second peak of DC_{60} in Fig. 19.

After t=0.03s, the reflected shock wave continues to propagate upstream along the intake and gradually deforms and attenuates within the curved duct. As the reflected shock wave gradually moves away from the blade region, the total pressure distribution at the AIP recovers to some extent compared with the strong shock-interaction stage. However, a certain degree of high- and low-total-pressure non-uniformity still exists within the section, indicating that shock-wave reflection and its interaction with the separated flow continue to disturb the exit flow field.

Overall, under the Z=5 condition, the shock wave also undergoes wall reflection, blade-region reflection, and interactions with the boundary layer and separated flow after entering the S-duct intake, resulting in unsteady variations in the average total pressure and DC_{60} at the AIP. However, owing to the larger scaled distance, the incident shock wave is relatively weaker. Therefore, the induced total-pressure fluctuations and dynamic distortion at the AIP are significantly lower than those under the Z=2 condition, and the influence on the intake-exit flow quality is relatively smaller.

4. Conclusion

This study addresses the dynamic distortion of an S-duct intake subjected to shock-wave loading. A three-dimensional unsteady numerical simulation method based on the Pressurized Bubble Method (PBM) and a blade-resolved MRF approach is established. The propagation and reflection of blast shock waves entering the S-duct intake at different scaled distances, as well as the induced evolution of dynamic distortion at the AIP, are investigated. The main conclusions are as follows:

1) By comparing the M2129 S-duct intake simulation with wind-tunnel experimental results, the capability of the present unsteady numerical method to predict the wall pressure distribution in the intake is validated. Meanwhile, the overpressure time history obtained using the PBM agrees well with the ideal detonation result, indicating that the PBM can accurately capture the propagation characteristics of blast shock waves and can be applied to the analysis of intake dynamic distortion under shock-wave loading.

2) After entering the S-duct intake, the shock wave undergoes multiple reflections and deformation under the combined effects of the curved walls, boundary layer, and separated flow. After interacting with the first-stage compressor blade region, an upstream-propagating reflected shock wave is formed. The propagation and reflection of the shock wave significantly alter the total pressure distribution at the AIP, producing pronounced transient non-uniformity in the exit flow field and causing a rapid increase in the dynamic distortion level accompanied by unsteady fluctuations.

3) For the scaled-distance case of Z=2, the incident shock wave is relatively strong. After the shock wave reaches the AIP, it causes a rapid increase in the average total pressure and strong fluctuations in DC_{60}. The reflection from the blade region and the circumferentially non-uniform disturbance induced by the blade rotational effect lead to an obvious asymmetric total pressure distribution at the AIP. The dynamic distortion continues to oscillate after the shock-wave impact, indicating that blast shock waves at small scaled distances can significantly deteriorate the flow quality at the intake exit.

4) For the scaled-distance case of Z=5, the shock wave also undergoes wall reflection, blade-region reflection, and interactions with the boundary layer and separated flow after entering the intake, resulting in unsteady variations in the average total pressure and DC_{60} at the AIP. However, owing to the increased scaled distance, the incident shock wave is relatively weaker. Therefore, the induced total pressure fluctuations and dynamic distortion at the AIP are significantly lower than those in the Z=2 case, and the influence on the intake-exit flow quality is relatively smaller.

Overall, blast shock-wave loading can induce strong dynamic distortion at the exit of an S-duct intake through shock-wave propagation, wall reflection, blade-region reflection, and interactions with complex internal flow structures. The results of this study provide a reference for analyzing the dynamic distortion mechanism of S-duct intakes under shock-wave loading, anti-distortion intake design, and propulsion system safety assessment.

5. Contact Author Email Address

Baigang Mi: mibaigang@nwpu.edu.cn

6. Copyright Statement

The authors confirm that they, and/or their company or organization, hold copyright on all of the original material included in this paper. The authors also confirm that they have obtained permission, from the copyright holder of any third party material included in this paper, to publish it as part of their paper. The authors confirm that they give permission, or have obtained permission from the copyright holder of this paper, for the publication and distribution of this paper as part of the ICAS proceedings or as individual off-prints from the proceedings.

7. Acknowledgement

This work is supported by the Natural Science Foundation of Chongqing (Grant No. CSTB2023NSCQ-MSX0042).

References

[1] Huang HX, Sun S, Yu H, et al. Recent Progress in Subsonic S-Shaped Inlets. Journal of Propulsion Technology, Vol. 41, No. 12, pp 2641-2658, 2020.

[2] Asadi D, Sabzehparvar M and Talebi H A. Damaged airplane flight envelope and stability evaluation. Aircraft Engineering & Aerospace Technology, Vol. 85, No. 3, pp. 186–198, 2013.

[3] Dunn M G, Padova C and Adams R M. Response of an operational turbofan engine to a simulated nuclear blast. Journal of Fluids Engineering, Vol. 109, No. 2, pp. 121–129, 1987.

[4] Guimarães T, Lowe KT and O'Brien WF. Vortical flow development in round ducts across scales for engine inlet applications. Experiments in Fluids, Vol. 60, No. 4, 2019.

[5] Seddon J and Goldsmith EL. Intake Aerodynamics. AIAA Education Series, 1985.

[6] Kingery CN and Bulmash G. Airblast Parameters from TNT Spherical Air Burst and Hemispherical Surface Burst. ARBRL-TR-02555, U.S. Army Ballistic Research Laboratory, 1984.

[7] U.S. Department of Defense. UFC 3-340-02: Structures to Resist the Effects of Accidental Explosions. 2008.

[8] Díaz JS and Rigby SE. Blast wave kinematics: theory, experiments, and applications. Shock Waves, Vol. 32, No. 5, pp 405-415, 2022.

[9] Synthetik Applied Technologies, LLC. blastFoam: An OpenFOAM Solver for Compressible Multi-Fluid Flow with Application to High-Explosive Detonation. 2019.

[10] Sohaimi ASM, Risby MS, Ishak SAFM, Khalis S, Norazman MN, Ariffin I and Yusof MA. Using Computational Fluid Dynamics (CFD) for Blast Wave Propagation under Structure. Procedia Computer Science, Vol. 80, pp 1202-1211, 2016.

[11] Li J and Hao H. Internal and external pressure prediction of vented gas explosion in large rooms by using analytical and CFD methods. Curtin University, 2017.

[12] Molkov VV, Cirrone DMC, Shentsov VV, Dery W, Kim W and Makarov DV. Dynamics of blast wave and

fireball after hydrogen tank rupture in a fire in the open atmosphere. International Journal of Hydrogen Energy, Vol. 46, No. 5, pp 4644-4665, 2021.

[13]Huang M, Wang P, Yao C, Cheng L, Ying W. A robust and efficient multi-physics numerical system for intensive blast wave propagation in complex environments. arXiv:2411.02407, 2024.

[14]Mohotti D, Wijesooriya K and Weckert S. A simplified approach to modelling blasts in computational fluid dynamics (CFD). Defence Technology, Vol. 23, pp 19-34, 2023.

[15]Dacko AK and Toczyski J. Structural response of a blast loaded fuselage. Journal of KONES, pp 101-109, 2010.

[16]Simmons MC and Schleyer GK. Pulse pressure loading of aircraft structural panels. Thin Walled Structures, Vol. 44, No. 5, pp 496-506, 2006.

[17]Agrawal R, Winkler C, Bose S and Moin P. Predictions of flow distortions inside a serpentine diffuser from large-eddy simulations. arXiv:2506.15646, 2025.

[18]Mayer DW, Anderson BH and Johnson TA. 3D subsonic diffuser design and analysis. Proc 34th AIAA/ASME/SAE/ASEE Joint Propulsion Conference and Exhibit, 1998.

[19]Li PR. Numerical Simulation of Propeller Jet Field Based on Star-CCM+. American Journal of Scientific Research and Essays, Vol. 5, 2020.

[20]Anderson JD. Fundamentals of Aerodynamics. McGraw-Hill, 2016.

[21]Menter FR, Kuntz M and Langtry R. Ten years of industrial experience with the SST turbulence model. Turbulence, 2003.

[22]Schmidt W and Bradley R. Air intakes high speed vehicles. Advisory Group for Aerospace Research and Development, AGARD-AR-270, Vol. 13, 1991.

[23]Blanc L, Santana Herrera S and Hanus JL. Simulating the blast wave from detonation of a charge using a balloon of compressed air. Shock Waves, Vol. 28, No. 4, pp 641-652, 2018.

[24]Luo JY, Issa RI and Gosman AD. Prediction of impeller-induced flows in mixing vessels using multiple frames of reference. Proc IChemE Symposium Series, No. 136, pp 549-556, 1994.

[25]Sommersel OK, Bjerketvedt DK, Christensen SO, Krest O and Vaagsaether K. Application of background oriented schlieren for quantitative measurements of shock waves from explosions. Shock Waves, Vol. 18, pp 291-297, 2008.